Optical analysis of tin-doped GaNAs layers grown on GaAs by molecular beam epitaxy

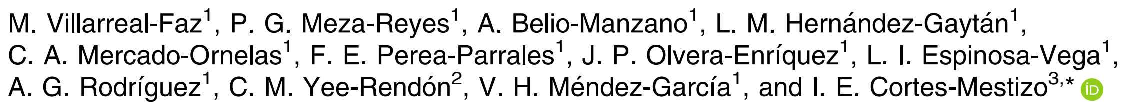

M. Villarreal-Faz[1], P. G. Meza-Reyes[1], A. Belio-Manzano[1], L. M. Hernández-Gaytán[1], C. A. Mercado-Ornelas[1], F. E. Perea-Parrales[1], J. P. Olvera-Enríquez[1], L. I. Espinosa-Vega[1], A. G. Rodríguez[1], C. M. Yee-Rendón[2], V. H. Méndez-García[1], and I. E. Cortes-Mestizo[3,*]

[1] *Coordinación para la Innovación y la Aplicación de la Ciencia y la Tecnología (CIACYT), Universidad Autónoma de San Luis Potosí, Av. Sierra Leona #550, Col. Lomas 2a Sección, 78210 San Luís Potosí, San Luis Potosí, México*

[2] *Facultad de Ciencias Físico-Matemáticas, Universidad Autónoma de Sinaloa, Av. de las Américas y Blvd. Universitarios, 80000 Culiacán, Sinaloa, México*

[3] *CONACYT-Coordinación para la Innovación y la Aplicación de la Ciencia y la Tecnología (CIACYT), Universidad Autónoma de San Luis Potosí, Av. Sierra Leona #550, Col. Lomas 2a Sección, 78210 San Luís Potosí, San Luis Potosí, México*

Received: 22 November 2022
Accepted: 28 February 2023
Published online:
23 March 2023

© The Author(s), under exclusive licence to Springer Science+Business Media, LLC, part of Springer Nature 2023

ABSTRACT

The optical non-destructive characterization of tin-doped GaN_xAs_{1-x} layer grown on GaAs (100) is presented. Molecular beam epitaxy was employed to grow GaNAs:Sn samples with nitrogen molar content at two different values, $x \sim 0.001$ and ~ 0.02. The n-type doping concentration was controlled by the Sn effusion cell temperature (T_{Sn}), exploring the range from 700 to 850 °C. High-resolution x-ray diffraction rocking curves of the samples indicate that it is possible to obtain GaNAs:Sn layers with appropriated crystallinity. Raman spectra present modifications in vibrational modes related to the Sn atom incorporation. The plasmon-phonon-coupled mode frequency and intensity are evaluated, showing a T_{Sn}-dependent donor atom concentration range from 10^{16} to 10^{19} cm^{-3}. Spectral signatures obtained by photoreflectance spectroscopy reveal an increasing E_{-} broadening parameter as the Sn effusion cell temperature is raised. Additionally, from Franz–Keldysh oscillations it is observed that the internal electric field strength increases with the donor concentration. The optical results were contrasted using the four-point probe method, demonstrating changes in sheet resistivity for the samples according with the employed spectroscopies. For similar T_{Sn}, the set of samples with $x \sim 0.02$ shows increased properties related to tin incorporation for each characterization technique.

Address correspondence to E-mail: irving.cortes@uaslp.mx

https://doi.org/10.1007/s10854-023-10195-2

1 Introduction

The semiconductor material gallium nitride arsenide (GaN_xAs_{1-x}) has attracted considerable interest for investigation and development, because the electronic band structure of GaAs can be radically modulated by introducing small quantities of Nitrogen atoms when the ternary compound is built up. The most prominent applications of the GaNAs are obtained when it is utilized in conjunction with GaAs and other III–V semiconductors compounds [1–5]. GaNAs sustain low lattice mismatch with GaAs within the dilute nitride regime ($x \leqq 0.03$) and has advantageous band structure behavior. Incorporation of nitrogen atoms in As lattice sites of the GaAs matrix produces the splitting of the conduction band edge into upper (E_+) and lower (E_-) energies [6, 7]. In the x range from 0 to 0.03 the GaNAs lattice constant is reduced around 0.5 Å [8].

Gallium nitride arsenide has been used in the development of novel optoelectronic devices capable of detecting and processing low photon energy [1–3]. The large bandgap scale of E_- and E_+ covers a wide range of the solar spectrum, making this III-N-V alloy a candidate for multi-junction solar cells [3, 9]. The GaNAs has been applied in the development of opto-spintronic semiconductor nanostructures [10]. The bandgap ranging from the near-infrared to infrared spectral region makes the GaNAs an ideal material for applications in light-emitting diodes and nano-lasers [11]. The GaAs/GaNAs/GaAs heterostructure can be added in the intrinsic region of p-i-n photodetectors to increase the photo-response for short energy photons [12].

Another interesting and important application of the GaNAs alloy is in the development of intermediate band solar cell [5]. For photovoltaics, E_- is planned to act as an intermediate band and E_+ would participate as the conduction band [5, 13]. This technology has been scarcely developed. The GaNAs employed as intermediate band material should exhibit an appropriate crystallinity when it is grown epitaxially on (Al, Ga)As. In addition, the interband process requires partially occupied E_- providing electrons to be excited toward the E_+ conduction band [13]. To expand the application of GaNAs to intermediate band solar cells, efforts in the improvement of its electrical properties while optimizing crystallinity are mandatory.

The rise of the nitrogen mole concentration leads to a significant detriment of the structural, optical, and electronic properties of GaNAs, compromising the efficiency of GaNAs-based devices' performance. Hence, the study of the growth of GaNAs is a permanent topic due to the fact that it plays a key role in determining the crystallinity. The growth of high-quality GaNAs alloys becomes more difficult for $x \leqq 0.02$ by the high miscibility gap between the constituent elements [14], complicating the incorporation of substitutional N atoms in the GaAs crystal and creating major difficulties for multilayered devices fabrication. One ex situ alternative to improve the structural properties and reduce the fraction of non-substitutional N atoms in the crystal is the application of rapid thermal annealing treatments [15, 16]. The annealing process of GaNAs has demonstrated to be an effective method to increase the substitutional nitrogen atoms, keeping the crystallinity and improving the optical properties [15, 16].

The charge carrier transport properties of the GaNAs also change with the incorporation of nitrogen atoms. For example, the electron effective mass and the scattering induced by the nitrogen mole composition percent (%N) result on electron mobilities in the order of a few hundred cm^2/Vs [17–19]. Improving the electrical properties of GaNAs layers is a major issue particularly for electronic and photovoltaics devices, conducting to multiple studies on the p- and n-type doping processes. For GaAs-based semiconductor materials, a wide number of donor and acceptor elements have been employed. Particularly, for n-type GaNAs silicon and selenium have been used as donors to dope in the range from 10^{17} to 10^{19} cm^{-3} [20–24], while p-type has been explored with zinc, magnesium, and beryllium atoms to obtain GaNAs doping in the range from 10^{16} to 10^{20} cm^{-3} [24, 25].

And while Si is typically selected for the MBE growth of n-type GaAs-based materials, it behaves amphoteric depending on growth conditions and substrate orientation [26]. For example, Silicon becomes an acceptor at low As/Ga flux ratio and a donor at high As/Ga flux ratio [26, 27]. In the MBE growth process of GaNAs, low As/Ga flux ratio and low temperature are employed to increase the nitrogen incorporation. Other donor elements with similar growth parameters but with lower amphoteric behavior than Silicon should be studied. In this effort, tin atoms have been employed for GaAs (100) n-type

grown with low As/Ga flux ratio and low substrate temperature, attaining high carrier concentration and avoiding surface segregation [27]. Consequently, Sn doping is a promising candidate to produce n-type GaNAs.

On the other hand, the E_- and E_+ bands formation in GaNAs makes difficult the proper determination of the transport properties due to the lack of information about ohmic contacts and the electron affinity for GaN_xAs_{1-x} if both conduction bands are accounted. In this task, non-contact and non-destructive techniques could be used for the analysis of the doping effect on the GaNAs alloy. For instance, spectroscopy techniques such as photoluminescence, photoreflectance (PR), and Raman (RS) have been proposed to estimate the impact of dopant incorporation on GaAs-based materials [22, 28, 29].

Here, GaNAs layers doped with Sn were grown by molecular beam epitaxy (MBE). RS and PR were employed to assess the tin incorporation on the GaNAs lattice grown with different nitrogen molar fractions. GaNAs:Sn/GaAs epilayers are achieved where the Sn incorporation is controlled by the tin effusion cell temperature. The frequency and intensity of vibrational modes on Raman spectra have been evaluated to find the influence of the donor atom concentration. A broadening of the E_- signature produced by the Sn incorporation was determined in conjunction with the presence of damping oscillations in the photoreflectance spectra. With this study, the authors showed a contactless strategy to quantify the Sn doping of GaNAs with the aim to overcome the requirement of ohmic contacts and to increase the employment of this III-N-V material in optoelectronic devices. Additionally, our intention is to contribute to the intermediate band cell concept by obtaining a n-type GaNAs alloy with appropriate crystallinity and optoelectronics properties.

2 Experimental

The III-N-V epilayers of this study were grown by solid-source molecular beam epitaxy on GaAs (100) semi-insulating epi-ready substrates using an Oxford-CNMX32 nitrogen radio-frequency plasma source for nitrogen supply. The temperature of Ga (7N5) and As (7N5) effusion cells was set to provide beam equivalent pressures of 3.7×10^{-5} and 1×10^{-3} Pa at 960 and 335 °C, respectively. Before the growth, surface oxides were desorbed in the MBE growth chamber under ultra-high vacuum environment by increasing the temperature up to 580 °C under As_4 overpressure. The growth began in all samples with a 150-nm-thick GaAs buffer layer deposited with a growth rate of 0.83 μm/h at desorption temperature.

Two nitrogen molar concentrations x of ~ 0.001 (samples A) and ~ 0.02 (samples B) were explored. For samples A, the nitrogen flux was set to 0.6 sccm, while the nitrogen power source was set at 250 W to produce a neutral atomic beam with negligible ion content [30]. The substrate temperature was kept at desorption temperature under N2 atmosphere during substrate thermalization, and the temperature of As was decreased to 230 °C. To improve the nitrogen incorporation for samples B, a nitrogen flux of 0.25 sccm with power of 350 W was employed in conjunction with a reduction in both temperatures: the As source to 220 °C and the substrate temperature 150 °C under desorption temperature.

To modulate the tin incorporation on GaNAs layers, the Sn (5N) effusion cell temperature (T_{Sn}) was varied in the range of 700 to 850 °C, which would correspond to GaAs n-type doping ranging from $\sim 10^{17}$ to $\sim 10^{19}$ cm^{-3} [31]. The Ga, Sn, and N shutters were opened simultaneously to grow 500-nm-thick GaNAs:Sn layers. Samples were labeled with a subscript indicating T_{Sn}, like A_{TSn} and B_{TSn}. For comparison purposes, two intrinsic GaNAs epilayers were also grown and identified as A_i and B_i.

For optical characterization, a micro-Raman system Horiba Xplora plus with the 532-nm laser line in backscattering geometry, 100-μm slit, and 100X microscope objective was employed. PR was carried out utilizing an experimental setup like those described elsewhere [32] with a laser wavelength of 635 nm with an optical power of 10 mW/cm^2 chopped at a frequency of 527 Hz. The probe beam comes from a tungsten–halogen lamp. The structural properties were studied using high-resolution x-ray diffraction (HRXRD) in a PANalytical Empyrean X-ray diffractometer with an emission line of 1.54056 Å. Lucas Lab S-302-4 mounting stand with 2601B Keithley system sourcemeter were utilized to get a four-point probe measurement of sheet resistivity.

3 Results

The fundamental physical properties and a wide variety of device applications make the fabrication and characterization of III-N-V materials interesting, particularly the GaNAs alloy. Nonetheless, to increase the %N content and to obtain reproducible high-quality GaNAs, thin films still require exhaustive research [33]. Here, HRXRD was employed to corroborate the %N on each set of samples. The (004) rocking curves of the GaNAs/GaAs intrinsic reference samples are displayed in Fig. 1. The diffractograms for both samples clearly show that the two peaks are related to the GaAs (at $\Delta\omega = 0°$) and the GaNAs (right side). The peak position associated with GaNAs (004) indicates a %N of 0.12 and 1.9 for A_i and B_i samples, respectively. The HRXRD curve of sample B_i exhibits a broad peak for the GaNAs layer, suggesting a lower crystal quality in comparison to A_i, probably due to the higher %N.

The diffraction pattern for B_{800} is also shown in Fig. 1. This case is analyzed given that both parameters, %N and T_{Sn}, could degrade the crystallinity of the ternary. Firstly, the peak associated with GaNAs is slightly closer to the GaAs peak, indicating a reduction of 0.1% in the nitrogen concentration, contrasted with the parameters exhibited by B_i. The modification of %N in the samples under study is probably associated with the growth process instead of effect of Sn incorporation. The maximum %N variation determined was of 0.1%, found for B_{800}. The differences observed by HRXRD in %N are likewise resolved by other spectroscopies, as it will be shown later. Thus, higher %N variations should produce important effects in the RS and PR spectra analysis, being necessary to be considered.

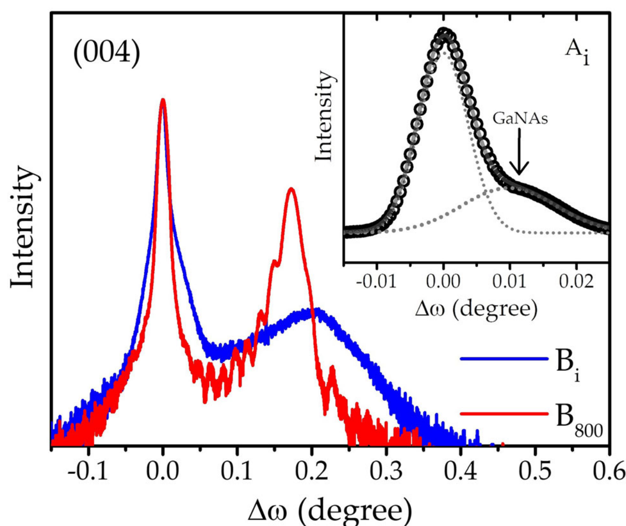

Fig. 1 (004) diffraction profile from B_i and B_{800} samples with %N of 1.9 and 1.8, respectively. The inset illustrates the diffractogram for A_i (open symbols) fitted to two Lorentzian peaks (solid line)

Additionally, the diffractogram of B_{800} exhibits Pendellösung fringes related to a high crystalline quality layer with a smooth and abrupt GaNAs/GaAs interface [33]. When epilayers are grown thick enough to relax significantly, an impressive diversity of effects is reported in the literature. This might signify that many parameters play an uncontrolled role, implying that plastic relaxation is essentially unpredictable like brittle failure and produces (or not) lattice disorder at high scale [34]. According to these, the different atomic radii of the atoms in the GaNAs:Sn alloy could have degraded the crystallinity during the relaxation process. Nevertheless, as stated by HRXRD, good crystallinity GaNAs films doped with Sn could obtain under appropriate growth conditions as the behavior obtained for sample B_{800}.

Figure 2a and b shows the Raman spectra for the samples under study prior to baseline treatment. A typical GaAs-based material Raman spectra display the first-order longitudinal optical (LO) mode, and it is exhibited by all samples as shown in Fig. 2 around 290 cm^{-1}. The intrinsic samples show the transverse optical (TO) mode. On the other hand, for the doped samples, the LO phonon couples with the plasma waves that originate the plasmon-phonon-coupled modes L_- and L_+ by the presence of high free carrier concentration [35]. Thus, tin-doped GaNAs RS show the L_- mode in Fig. 2 and their intensity increases as T_{Sn} does, supporting that the n-type doping was achieved. The L_- properties are employed to evaluate the tin doping formation as it will be shown.

At frequencies higher than 400 cm^{-1}, the Raman spectra display vibrational modes related to GaN and GaAs compounds. The presence of nitrogen in the samples is determined through the Nitrogen local vibration mode (*LVM*) located in $\sim$ 470 cm^{-1}, shaped by GaN-like TO_2 and LO_2 modes [15, 36]. Consequently, the *LVM* proves the incorporation of Nitrogen atoms into the GaAs lattice for the samples under study. The increase of the T_{Sn} also enlarges the

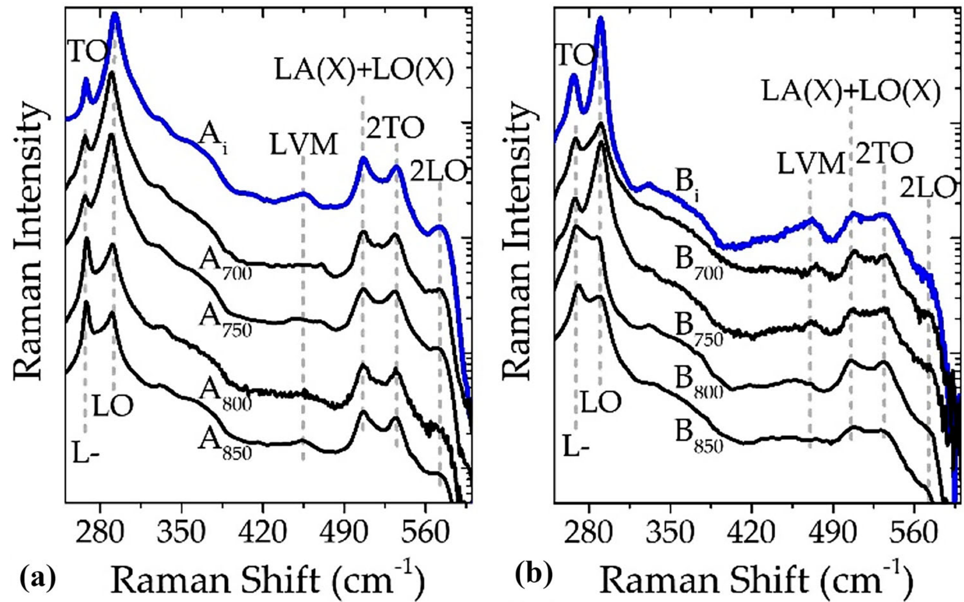

Fig. 2 Raman spectra at room temperature for **a** *A*-set and **b** *B*-set of samples under study. The Raman intensity has been normalized to the GaAs-LO mode intensity and exhibited in logarithmic scale. The dashed lines indicate the phonon region frequency for sake of clarity

fluorescence effect on the Raman spectra, covering up the intensity resolution of the vibrational modes, especially the *LVM* mode. The spectra of GaAs-based materials are complemented in the spectral region from 490 to 600 cm^{-1} by the presence of LA(X) + LO(X) and second-order scattering GaAs, like phonons modes [36].

Figure 3a shows the RS from A_i and B_i samples after baseline removal for two spectral regions with the aim to discern the effects of N incorporation from those produced by the Sn doping. In the region from 240 to 320 cm^{-1} a weak intensity TO mode around 267.5 cm^{-1} is resolved, while LO modes are located at 292.9 and 289.64 cm^{-1} for A_i and B_i, respectively. From 425 to 600 cm^{-1}, the spectrum shows the *LVM* around 470 cm^{-1} for both samples (inset of Fig. 3a). The RS was fitted by 2- and 5-peak Lorentzian curves for the described modes at each region with a minimum R-square of 0.98 to detect changes in the mode's intensity and frequency.

The TO integrated intensity (I_{TO}) for a perfect (100) zincblende lattice in a RS measured in backscattering geometry has to be null. Therefore, the I_{TO} is related to lattice disorder produced by the incorporation of N in the GaAs-host lattice, and it may rise as the %*N* increases [16]. Taking the LO mode integrated intensity (I_{LO}), the I_{LO}/I_{TO} ratio can be employed as a measurement of the lattice disorder produced by the %*N* in the intrinsic samples [15]. Thus, I_{LO}/I_{TO} of 27.4 and 2.7 were determined for the A_i and B_i samples, in that order. This indicates that higher nitrogen content in the GaNAs alloy produces larger lattice disorder, prior to the Sn incorporation.

The nitrogen concentration is estimated from the integrated intensity of the *LVM* (I_{LVM}) and I_{LO} modes by $[N] = I_{LVM}/(1.3I_{LO} + I_{LVM})$ [16, 36], finding %*N* = 1.1 and 2.15 for samples A_i and B_i, respectively. However, any estimation based on the integrated intensity of Raman modes is susceptible to errors originated from the data treatment, especially baseline subtraction. Alternatively, the frequency mode (ω) can be employed to analyze the influence of %*N* on RS. Nitrogen alloying produces changes in lattice parameters noted in RS as variations in the ω_{LO}, red shifting as %*N* increases [16, 37, 38]. Additionally, ω_{LO} is modified by residual strain. A red shift on ω_{LO} is linked to tensile strain in the epilayer ($\varepsilon > 0$) [15, 39]. On the other hand, ω_{TO} shifts occasionally by changes in %*N* in the ternary that can be discarded according to references [15, 16], which is corroborated in Fig. 2 and in Fig. 3a close to 267.5 cm^{-1} for intrinsic samples.

As shown in Fig. 3a, ω_{LO} red shifts in B_i contrasted with sample A_i due to tensile stress related to nitrogen-induced lattice disorder. The strain of the GaNAs/GaAs epilayer is estimated using $\omega_{LO} - \omega_0 = -1.3\omega_0\varepsilon$ [15, 39], where ω_0 is the unstrained GaAs-LO frequency mode. Values of ε = 0.15×10^{-3} and 6.45×10^{-3} were estimated for samples A_i and B_i, respectively. Under the

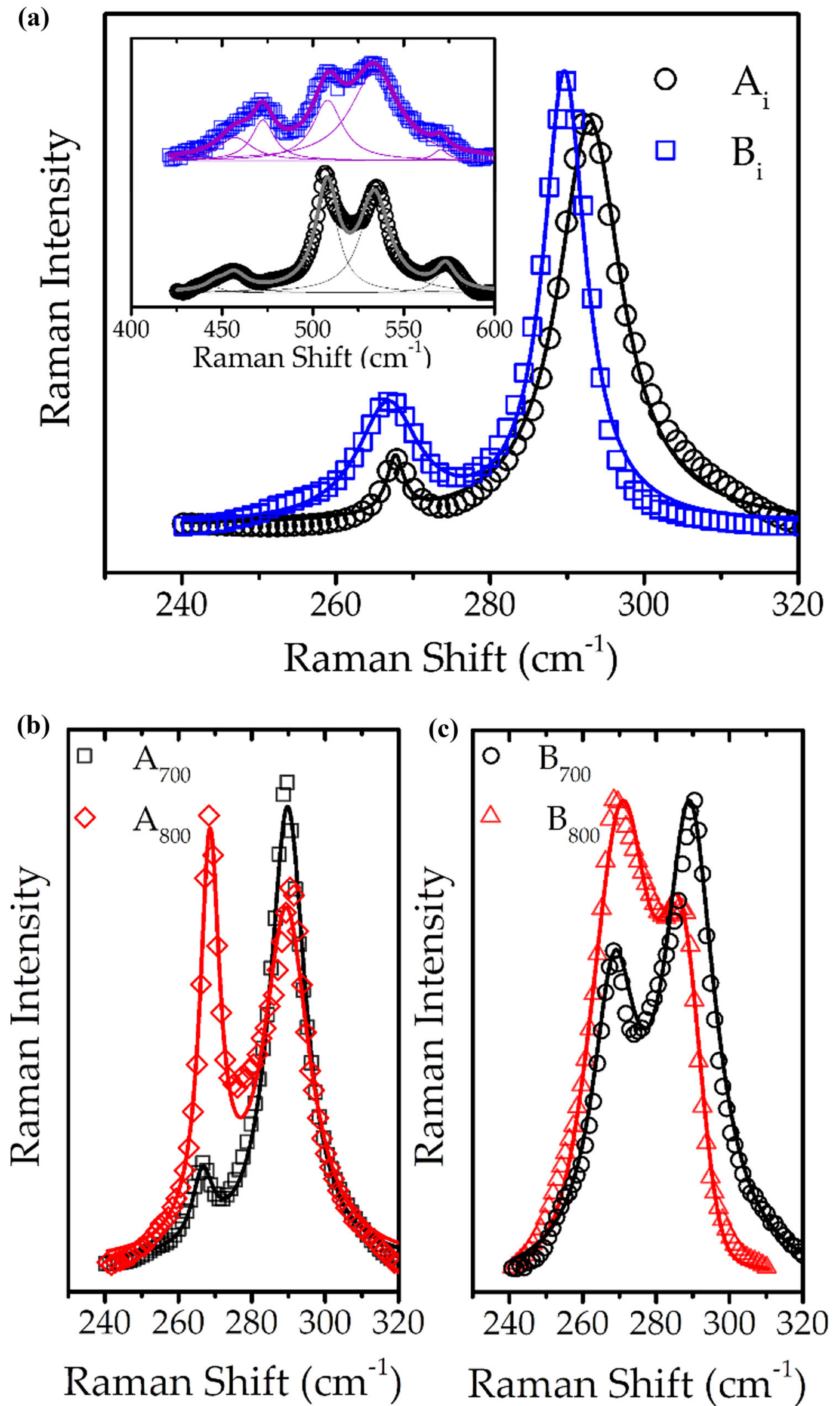

Fig. 3 Raman spectra for **a** A_i and B_i intrinsic samples. The inset shows the region from 400 to 600 cm^{-1} of intrinsic samples where the *LVM* is observed. Raman measurement for tin-doped samples at T_{Sn} = 700 and 800 °C from **b** *A*- and **c** *B*-type samples. Experimental data are plotted in open symbols, while solid lines indicate the fitting results

assumption that in the epilayer is mainly produced by the GaNAs/GaAs lattice mismatch and from the relationship between the lattice parameters of the substrate (a_S) and layer (a_L) in $\varepsilon = (a_S - a_L)/a_L$, the GaNAs lattice constant can be determined as well as $\%N$ [15, 40]. $\%N$ of 0.08 and 2.4% are found for A_i and B_i samples, respectively, which is in better agreement with HRXRD characterization than the RS I_{LO}/I_{TO} intensity ratio procedure.

Figure 3b and c demonstrates the effect of the introduction of tin in the GaNAs lattice through RS for selected T_{Sn}. As T_{Sn} increases the number of donor atoms (N_D) in the GaNAs also does, being L_- intensity (I_{L-}) larger for T_{Sn} of 800 °C than for 700 °C for both $\%N$ studied. I_{L-} compared with I_{LO} is different for the A and B samples even at the same T_{Sn}, perhaps result of the I_{TO} addition at I_{L-}. ω_{L-} was reported to blue shift when the free carrier concentration increases for GaAs-based materials [35, 41], which agrees with the ~ 2 cm^{-1} blue shift in ω_{L-} when changing T_{Sn} from 700 to 800 °C. A slight modification in ω_{LO} also is perceived for sample B_{800} product of the $\%N = 1.8$ described in Fig. 1.

Another demonstration of the Sn incorporation to GaNAs to form n-type doping is obtained by analyzing the samples near surface. The depletion layer width (D_L) at the surface produces ionized atoms, whose effects can be measured by I_{LO} [42]. In the RS spectra exhibited in this work, the laser line penetration (d) is around 120 nm [15, 43]. Hence, the contribution of the bulk is negligible, and I_{LO} is principally associated with D_L [42, 43]. D_L thickness is calculated through I_{LO} and I_{L-} by the equation $R = R_0[e^{2D_L/d} - 1]$, where $R = I_{LO}/I_{L-}$ and $R_0 = 1.44$ [42–44]. A D_L reduction from 115.3(35.6) to 52.7(9.2) nm was determined for sample $A(B)$ when T_{Sn} is raised from 700 to 800 °C. N_D augmentation involves larger quantity of free carriers that fill the surface states, dropping the D_L thickness [45].

Moreover, the doping level should not modify the surface state density [45]. Under this consideration, each sample should sustain very similar surface state energy levels, typically positioned at mid-gap for GaAs-based materials [45, 46]. These usual parameters produce a band bending with a surface barrier height of $\phi_{ss} = 0.72$ eV for GaAs [42]. The Fermi level for GaN is reported to be pinned 0.5–0.7 eV below the conduction band minimum [46]. Assuming by the dilute nitride regime the GaAs properties, from $\phi_{ss} = qN_D{D_L}^2/2\epsilon_0\epsilon_r$, where q is the electron charge, ϵ_0 is the vacuum dielectric constant, and ϵ_r is the static dielectric constant, the N_D can be estimated [47], being of 7.8×10^{16} (3.1×10^{17}) cm^{-3} and 8.7×10^{17} (1.2×10^{19}) cm^{-3} for T_{Sn} at 700 and 800 °C, respectively, in samples $A(B)$.

PR spectroscopy has been employed to analyze the band structure of the GaNAs system [15, 48]. Additionally, this technique is used to determine the electric field strength and distribution in GaAs-based devices [40, 45, 48]. Figure 4 shows the PR spectra of the samples under study to analyze the impact of the Sn doping. Lorentzian line shapes in PR spectrum are

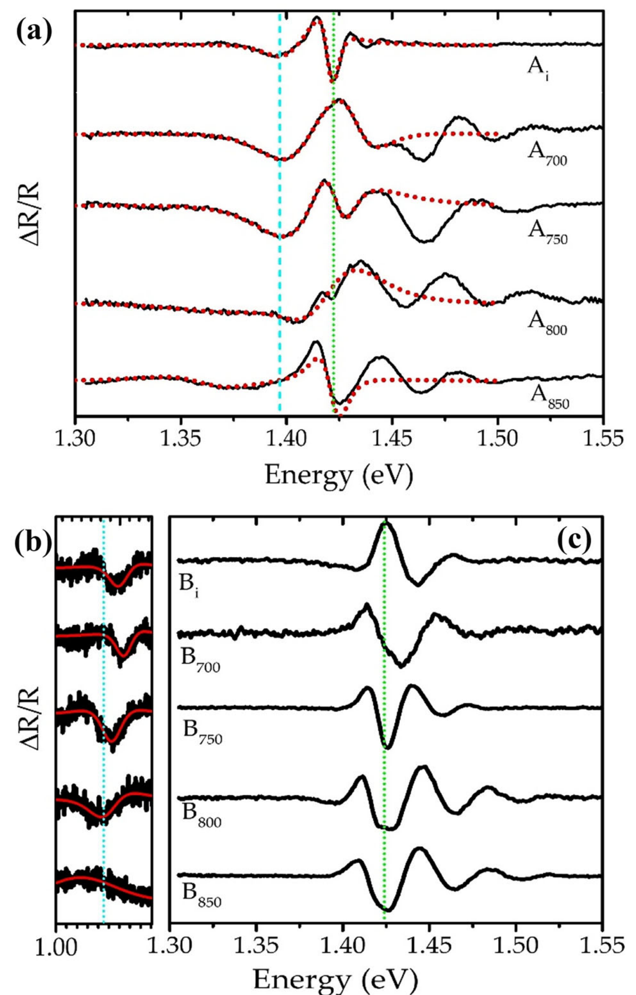

Fig. 4 Photoreflectance spectra for the **a** A set at the T_{Sn} explored. PR of samples B taken with **b** Ge detector in the region where E_- is expected and **c** with Si detector around E_0. The experimental data are shown in black-solid line, while the red plot corresponds to fittings with Eq. 1

present and associated to critical points of the GaNAs system (E_-) and GaAs (E_0). They are modeled using Aspnes' third derivate functional formula,

$$\frac{\Delta R}{R}(E) = \mathrm{Re}\left[\sum_{j=1}^{n} A_j e^{-i\phi_j}\left(E - E_j + i\Gamma_j\right)^{-m}\right]. \quad (1)$$

Here, n is the number of optical transitions considered, E_j is the critical point energy, Γ_j is the broadening parameter, A_j and φ_j are the amplitude and phase factor, respectively [49]. The m parameter is depending on the type of optical transition, and it was set to be 2.5 [15, 45, 48, 49].

Figure 4a displays the PR spectra of the GaNAs/GaAs system for samples A. Given the $\%N$ in the A set the E_- signature is located at 30 meV below E_0 (green dotted lines in Fig. 4), according to HRXRD and the band-anticrossing model [48]. Thus, overlapping effects can be expected within the spectral region where both gaps should be revealed [15]. The spectral features between 1.35 and 1.45 eV in Fig. 4a have been fitted by Eq. 1 with j = 2 with the aim to determine the E_- transitions. On the other hand, for $\%N$ = 1.9 E_- is estimated at 1.15 eV. In Fig. 4b, the E_- spectral region for Samples B, fitted with Eq. 1 with j = 1, is represented. The fittings are displayed with red lines in Fig. 4a and b. The E_- position (cyan dotted lines in Fig. 4) was found around 1.39 eV in A set with low variations between samples, indicating similar $\%N$ for this grown process. Otherwise, for B samples modifications around 30 meV were found with an average position of 1.16 eV for E_-.

The influence of the Sn n-type doping on the PR spectra of GaNAs layers is analyzed by the broadening parameter of the E_- signal, Γ_{E-}. The Γ_j is also estimated from the fitting process and usually is an indicator of crystallinity grade [15, 48]. The PR signal associated with E_- becomes wider as T_{Sn} increases in the A set. Similar and stronger behavior is observed for B samples where the E_- line shape changes are more notorious. The broadening for $A_i(A_{850})$ and $B_i(B_{850})$ estimated is 0.020(0.042) and 0.070(0.285) eV, respectively. Thus, the Γ_{E-} extent is consequence of changes in the crystallinity and/or to the doping effect. For example, in B_{800} the Γ_{E-} of 0.101 eV suggests lower crystallinity for the Sn inclusion in comparison of the intrinsic case. However, this broadening parameter relationship seems to be contrary to the crystal quality evaluated for B_i and B_{800} by HRXRD (Fig. 1). Consequently, the widening of E_- for the samples analyzed in this work is because of the doping process. Similar broadening parameter is reported in Ref. 28 for E_0 in GaAs-doped samples.

Figure 4a and c shows the PR spectra in the region from 1.3 to 1.5 eV. For the GaNAs/GaAs epilayers, the GaAs bandgap transition dominates the spectra. For GaNAs:Sn/GaAs samples the PR reveals features like damping oscillations above E_0 energy. The line shape of the PR spectra for energies over 1.42 eV in Fig. 4a and c is considered as FKO and could be related with electric fields associated with the doping level in samples or equivalently with T_{Sn}. The presence of Franz–Keldysh oscillations (FKO) in Fig. 4a and c allows the determination of built-in electric fields (E_{int}) in the samples [40]. The $\Delta R/R$ in the intermediate field case of this modulation spectroscopy is analyzed by the Aspnes and Studna expression [50],

$$\frac{\Delta R}{R} \propto \cos\left(\frac{2}{3}\left[\frac{E - E_j}{\hbar\Omega}\right]^{3/2} + \varphi_j\right), \quad (2)$$

where $\hbar\Omega$ is the characteristic electro-optic energy

$$\hbar\Omega = \left(\frac{q^2 E_{\mathrm{int}}^2 \hbar^2}{2\mu}\right)^{\frac{1}{3}}. \quad (3)$$

In Eq. 3 the μ is the interband reduced mass involved in the direction of the field.

The FKO frequency is related to the E_{int} strength. To determine the E_{int} strength the asymptotic Franz–Keldysh modulation theory was used. From Eq. 2 an n-th extremum of the FKO from the $\Delta R/R$ spectra occurs if the cosine argument reaches a value of $j\pi$. A linear graph can be obtained by plotting the energy that corresponds to each extremum vs. the index j, and from the slope of the fitted line the value of $\hbar\Omega$ can be determined to obtain the E_{int} strength, using Eq. 3, standard procedure indicated elsewhere in the literature [47, 51].

The calculated electric field indicated that the larger the T_{Sn}, the stronger is E_{int}. When the photogenerated minority carriers recombine with the charge trapped on the surface or at the interface states, the electric field distribution along the sample is modulated [45]. Therefore, in GaNAs/GaAs samples, the FKO should have been originated from surface or interface charge density modulation. A greater electron charge concentration is expected in the trap

states coming from donor atoms. The larger the T_{Sn}, the bigger number of electrons trapped, producing a higher electric field modulation by the laser line, which results in an increase of the FKO period with clear damping oscillations spectra, as it is noted in Fig. 4a and c confirming the n-type GaNAs material.

The experimental data showed by Raman and photoreflectance displayed modifications associated to tin doping of GaNAs, allowing to assess the insertion of Sn in the GaNAs lattice. Further, it is necessary to compare the electrical measurements taking into account the differences produced by the physical characteristics of each technique. The four-probe method for measuring semiconductor resistivity allows for non-destructive measurements meant to evaluate the sheet resistivity ($\rho_{\square}$) dependence of the samples with T_{Sn}. For both intrinsic samples $\rho_{\square}$ = 40 KΩ/sq was determined.

The result for the A and B set of doped samples is presented in Fig. 5a where the sheet resistance decreases with increasing T_{Sn} in comparison with the intrinsic $\rho_{\square}$ values. The lowest $\rho_{\square}$ of 11.5 and 0.22 KΩ/sq were found for A_{800} and B_{800}, respectively, being the A set of samples more resistive than the B series. The $\rho_{\square}$ dependence in Fig. 5a is evidence that the n-type doping formation is established by Sn atoms in the GaNAs lattice, providing carriers that reduce the resistivity of the dilute nitride material. The electrical properties of the GaNAs are also modulated by %N, i.e., low(high) nitrogen concentration reduces(rises) the intrinsic carrier concentration while rises (reduces) the mobility [52, 53]. Since both parameters affect the resistivity $\rho_{\square}$, it is similar for A_i and B_i. Additionally, the reduction in the electron mobility induces high resistivity range for A samples.

Figure 5b shows the donor density N_D as a function of T_{Sn} employed in each set of samples, resulting from the Raman mode intensity analysis. Samples of set A exhibit a clear tendency, N_D increases as T_{Sn} does and gets the higher rate at 850 °C with 4.7×10^{17} cm^{-3}. On the other hand, the dependence is not clear for B samples where the N_D maximum is reached at 800 °C. The N_D lowest value is found for B_{750}. As depicted in Fig. 2b the RS measurement for B_{750} suggests that the L_- did not show the expected trend, probably because of the growth process. In the interpretation of N_D through RS spectrum some parameters can alter the doping estimation, i.e., a higher %N should affect the estimation by adding I_{TO}

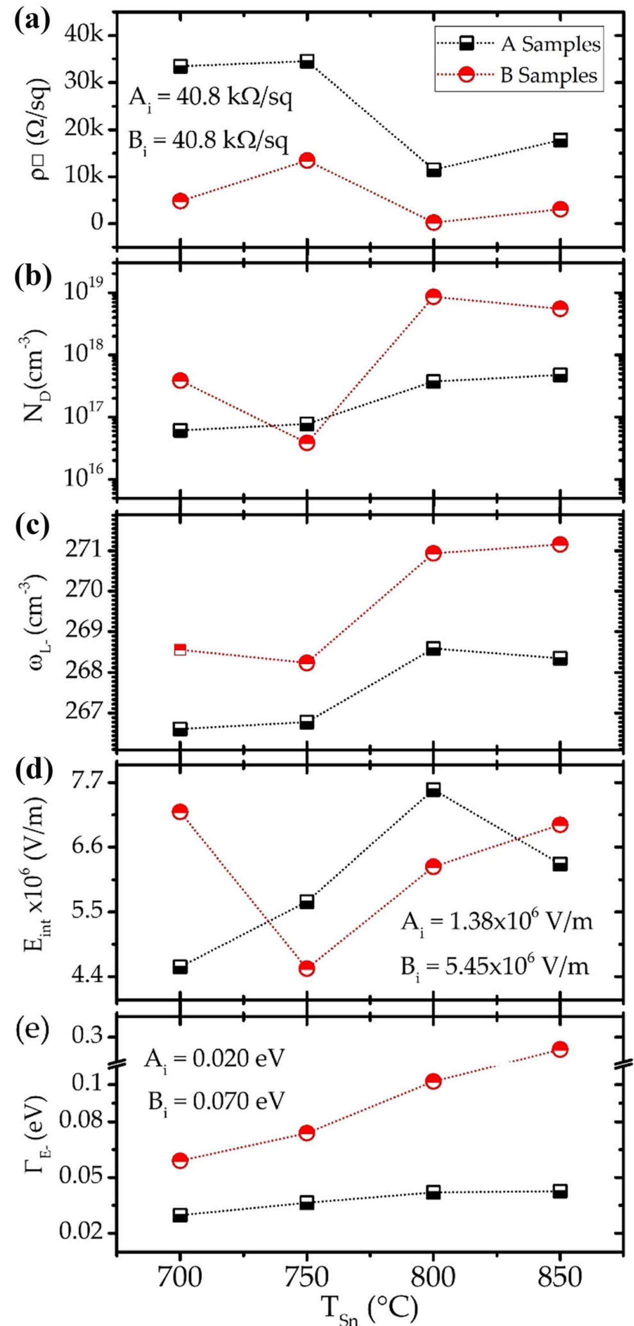

Fig. 5 GaNAs properties found for doped and non tin-doped samples: **a** $\rho_{\square}$ sheet resistivity obtained through four-point measurements, **b** N_D donor concentration, and **c** L_- mode frequency behavior given by Raman spectroscopy. PR spectroscopy allowed to obtain the **d** magnitude of the electric field through the analysis of the FKO and **e** the E_- broadening parameter as a function of T_{Sn}

on I_{L-}. The ω_{L-} dependence on T_{Sn} is displayed on Fig. 5c. ω_{L-} blue shifts as T_{Sn} rises, except for A_{850} and B_{750} where a reduction in frequency is detected.

For higher Sn concentration, the L_+ mode intensity may become important and change the line shape of the LO mode, hindering the data fitting process. Accordingly, the ω_{L-} behavior depicts similar results to those obtained for the $\rho_\square$ values plotted in Fig. 5a.

The E_{int} obtained by the FKO induced by T_{Sn} in the PR spectra is illustrated in Fig. 5d. The maximum E_{int} magnitude for A_{800} and B_{700} is around 7×10^6 V/m. E_{int} increases as the T_{Sn} rises because of the change in the carrier density distribution along the epilayer. In multilayered systems, the FKO line shape is an interference pattern from the contribution of each electric field along the epilayers and heterostructures, introducing some uncertainty in the E_{int} estimation. Figure 5e gathers the behavior of Γ_{E-} with T_{Sn}. Γ_{E-} specifies that the maximum(minimum) donor concentration is found for samples $A_{800}(A_{700})$ and $B_{850}(B_{700})$ in concordance with the techniques on Fig. 5.

According to Fig. 5, the data from each characterization technique meant to quantify the tin doping of GaNAs, exhibited slight variations between them. Series A shows a similar trend in Fig. 5 plots, in comparison with the line shape of B samples. PR and RS demonstrate dissimilar trends. Each technique to estimate the Sn doping concentration is affected by $\%N$. Consequently, the behavior obtained for the A series, low nitrogen concentration, is more reproducible with the methods explored here than the obtained for the B samples, where higher nitrogen concentration is present.

4 Conclusion

N-type doping with Sn atoms in the GaNAs alloy is demonstrated by this work through non-destructive techniques. The plasmon-phonon-coupled mode in its integrated intensity and frequency peak appears to be sensitive enough to determine the Sn incorporation, since both parameters increase with the donor atom concentration. The photoreflectance spectra provide information related to Sn doping when the line shape is analyzed. The number of incorporated donor atoms changes the charge distribution calculated through Franz–Keldysh oscillations. The spectral signature associated to E_- broadens with the inclusion of Sn. For similar T_{Sn}, the $\%N \sim 2$ illustrates higher rates for the parameters evaluated in each methodology than the A series. Through this study the authors presented a strategy to assess and quantify the Sn doping on GaNAs by the employment of photoreflectance and Raman spectroscopies, examining their advantages and drawbacks with the aim to present alternative ways to analyze GaNAs-based materials avoiding the difficulty to obtain ohmic contacts.

Acknowledgements

The authors acknowledge to CONACYT program Investigadoras e Investigadores por Mexico (Project No. 44). The authors also thank IrinaVlaeva for professional English editing service.

Author contributions

Thin-film preparation, characterization, and writing of the manuscript were realized by all the authors. Data collection and analysis were performed by MVF and PGMR. IECM contributed to the conceptualization, supervision, and editing of the manuscript. All authors read and approved the final manuscript.

Funding

The authors acknowledge the financial support of FRC-UASLP, COPOCyT, and CONACYT-Mexico through grants: INFR-2015-01-255489, CB 2015-257358, PNCPN2014-01-248071, and Fideicomiso 23871.

Data availability

The datasets generated during the current study are available from the corresponding author on reasonable request.

Declarations

Conflict of interest The authors declare that they have no known competing financial interests or personal relationships that could have appeared to influence the work reported in this paper.

Ethical approval This paper meets the ethical standards of this journal.

References

1. M. Yukimune, R. Fujiwara, F. Ishikawa, S. Chen, W.M. Chen, I.A. Buyanova, *Compound Semiconductor Week (CSW)* (IEEE, New York, 2019), pp.1–1
2. C.K. Tan, D. Borovac, W. Sun, N. Tansu, S. Preuss, Sci. Rep. 6, 19271 (2016). https://doi.org/10.1038/srep19271
3. W. Dawidowski, B. Ściana, K. Bielak, M. Mikolášek, J. Drobný, J. Serafińczuk, I. Lombardero, D. Radziewicz, W. Kijaszek, A. Kósa, M. Florovič, J. Kováč Jr., C. Algora, L. Stuchlíková, Energies 14(15), 4651 (2021). https://doi.org/10.3390/en14154651
4. F. Sarcan, Y. Wang, T.F. Krauss, T. Erucar, A. Erol, Opt. Laser Technol. 122, 105888 (2020). https://doi.org/10.1016/j.optlastec.2019.105888
5. P. Prete, N. Lovergine, Prog Cryst. Growth Charact. Mater. 66(4), 100510 (2020). https://doi.org/10.1016/j.pcrysgrow.2020.100510
6. R. Kudrawiec, G. Sek, J. Misiewicz, L.H. Li, J.C. Harmand, Solid State Commun. 129(6), 353–357 (2004). https://doi.org/10.1016/j.ssc.2003.11.004
7. W. Shan, W. Walukiewicz, K.M. Yu, J.W. Ager III., E.E. Haller, J.F. Geisz, D.J. Friedman, J.M. Olson, S.R. Kurtz, H.P. Xin, C.W. Tu, Phys. Stat. Sol (b) 223, 75 (2001)
8. S.Z. Wang, S.F. Yoon, W.J. Fan, W.K. Loke, T.K. Ng, S.Z. Wang, J. Appl. Phys. 96, 2010 (2004). https://doi.org/10.1063/1.1767614
9. Md.D. Haque, Md.H. Ali, Md.M. Hossain, Md.S. Hossain, M.I. Hossain, Md.A. Halim, A.Z.M.T. Islam, Phys. Scr. 97(8), 085006 (2022). https://doi.org/10.1088/1402-4896/ac7d79
10. Y. Huang, V. Plojärvi, S. Hiura, P. Höjer, A. Aho, R. Isoaho, T. Hakkarainen, M. Guina, S. Sato, J. Takayama, I.A. Buyanova, W.M. Chen, Nat. Photonics 15, 475–482 (2021). https://doi.org/10.1038/s41566-021-00786-y
11. J.E. Stehr, R.M. Balagula, M. Jansson, M. Yukimune, R. Fujiwara, F. Ishikawa, W.M. Chen, I.A. Buyanova, Nanotechnol 31(6), 065702 (2019). https://doi.org/10.1088/1361-6528/ab51cd
12. K.A. Mohamada, M.S. Nordinb, N. Nayana, A. Aliasc, A.R. Mohmadd, A. Boland-Thomsb, A.J. Vickersb, Characterization of III-V dilute nitride based multi-quantum well pin diodes for next generation opto-electrical conversion devices. Mater. Today Proc. 7, 625–631 (2019). https://doi.org/10.1016/j.matpr.2018.12.053
13. N. Ahsan, N. Miyashita, M.M. Islam, K.M. Yu, W. Walukiewicz, Y. Okada, Appl. Phys. Lett. 100, 172111 (2012). https://doi.org/10.1063/1.4709405
14. M. Yukimune, R. Fujiwara, T. Mita, N. Tsuda, J. Natsui, Y. Shimizu, M. Jansson, R. Balagula, W.M. Chen, I.A. Buyanova, F. Ishikawa, Nanotechnol 30(24), 244002 (2019). https://doi.org/10.1088/1361-6528/ab0974
15. J.J. Cabrera Montealvo, L.I. Espinosa Vega, L.M. Hernández Gaytán, C.A. Mercado Ornelas, F.E. Perea Parrales, A. Belio Manzano, C.M. Yee, A.G. Rendón, V.H. Rodríguez, I.E. Méndez García, Cortes, Mestizo, Thin Solid Films 748, 139147 (2022). https://doi.org/10.1016/j.tsf.2022.139147
16. H.F. Liu, N. Xiang, S.J. Chua, S. Tripathy, J. Cryst. Growth 288(1), 44–48 (2006). https://doi.org/10.1016/j.jcrysgro.2005.12.045
17. I. Suemune, K. Uesugi, T.Y. Seong, Semicond. Sci. Technol. 17, 755–761 (2002). https://doi.org/10.1088/0268-1242/17/8/303
18. J. Olea, K.M. Yu, W. Walukiewicz, G. Gonzalez-Díaz, Phys. Status Solidi C **7**(7–8), 1890–1893 (2010). https://doi.org/10.1002/pssc.200983569
19. L. Wang, O. Elleuch, Y. Shirahata, N. Kojima, Y. Ohshita, M. Yamaguchi, J. Cryst. Growth 437, 6–9 (2016). https://doi.org/10.1016/j.jcrysgro.2015.12.011
20. M. Shafi, R.H. Mari, M. Henini, D. Taylor, M. Hopkinson, Phys. Status Solidi C 6(12), 2652–2654 (2009). https://doi.org/10.1002/pssc.200982561
21. T. Tsukasaki, R. Hiyoshi, M. Fujita, T. Makimoto, J. Cryst. Growth 514, 45–48 (2019). https://doi.org/10.1016/j.jcrysgro.2019.02.042
22. T. Tsukasaki, R. Hiyoshi, M. Fujita, T. Makimoto, Cryst. Res. Technol. 56(3), 2000143 (2021). https://doi.org/10.1002/crat.202100204
23. J. Ibáñez, E.A. Lladó, R. Cuscó, L. Artús, D. Fowler, A. Patanè, K. Uesugi, I. Suemune, J. Mater. Sci. Mater. Electron. 20, 425–429 (2009). https://doi.org/10.1007/s10854-008-9661-x
24. S.W. Johnston, S.R. Kurtz, J. Vac Sci. Technol. A 24, 1252 (2006). https://doi.org/10.1116/1.2167081
25. M. Shiraga, Y. Nakai, T. Hirashima, A. Kittaka, M. Ebisu, N. Takahashi, T. Noda, M. Ohmori, H. Akiyama, N. Tsurumachi, S. Nakanishi, H. Miyagawa, H. Itoh, S. Koshiba, Phys. Status Solidi C 8(2), 420–422 (2011). https://doi.org/10.1002/pssc.201000595
26. A.N. Klochkov, G.B. Galiev, E.A. Klimov, S.S. Pushkarev, Phys. Status Solidi b 260(2), 2200297 (2022). https://doi.org/10.1002/pssb.202200297
27. S.J. Hu, M.R. Fahy, K. Sato, B.A. Joyce, J. Electron. Mater. 24(8), 1003–1006 (1995). https://doi.org/10.1007/BF02652974

28. L. Peters, L. Phaneuf, L.W. Kapitan, W.M. Theis, J. Appl. Phys. 62, 4558 (1987). https://doi.org/10.1063/1.339050
29. N.I. Goktas, E.M. Fiordaliso, R.R. LaPierre, Nanotechnol 29(23), 234001 (2018). https://doi.org/10.1088/1361-6528/aab6f1
30. H. Eshghi, F.S. Tehrani, J. Optoelectron, Adv. Mater. 11(10), 1467–1470 (2009)
31. A.Y. Cho, Thin Solid Films 100(3), 291–317 (1983). https://doi.org/10.1016/0040-6090(83)90154-2
32. J. Misiewicz, R. Kudrawiec, G. Sek, *Dilute Nitride Semiconductors*, 1st edn. (Elsevier, Wroclaw, 2005), pp. 279–324, https://doi.org/10.1016/B978-008044502-1/50009-3
33. A. Pulzara Mora, M. Meléndez Lira, C. Falcony Guajardo, M. López López, M.A. Vidal, S. Jiménez-Sandoval, M.A. Aguilar, Frutis, J. Vac Sci. Technol. B 24, 1591 (2006). https://doi.org/10.1116/1.2201451
34. D.J. Dunstan, J. Mater. Sci. Mater. Electron. 8, 337–375 (1997). https://doi.org/10.1023/A:1018547625106
35. O. T.Tite, M. Pagès, J.P. Ajjoun, D. Laurenti, E. Bormann, O. Tournié, M.C. Maksimov, Tamargo, Solid State Electron 47(3), 455–460 (2003). https://doi.org/10.1016/S0038-1101(02)00388-X
36. M. Ramsteiner, D.S. Jiang, J.S. Harris, K.H. Ploog, Appl. Phys. Lett. 84, 1859 (2004). https://doi.org/10.1063/1.1669070
37. J. Ibáñez, E.A. Lladó, R. Cuscó, L. Artús, M. Hopkinson, J. Appl. Phys. 102, 013502 (2007). https://doi.org/10.1063/1.2749491
38. H.F. Liu, N. Xiang, S. Tripathy, S.J. Chua, Thin Solid Films 515, 759–763 (2006). https://doi.org/10.1016/j.tsf.2005.12.282
39. T.P. Humphreys, J.B. Posthill, K. Das, C.A. Sukow, R.J. Nemanichi, N.R. Parikh, A. Majeed, J. Appl. Phys. 28, L1595 (1989). https://doi.org/10.1143/JJAP.28.L1595
40. J. Misiewicz, P. Sitarek, G. Sęk, R. Kudrawiec, J. Mater. Sci. 21(3), 263–320 (2003)
41. H. Altan, X. Xin, D. Matten, R.R. Alfano, Appl. Phys. Lett. 89, 052110 (2006). https://doi.org/10.1063/1.2236300
42. V.N. Bessolov, M.V. Lebedev, D.R.T. Zahn, J. Appl. Phys. 82, 2640 (1997). https://doi.org/10.1063/1.366079
43. I.E. Cortes Mestizo, L.I. Espinosa Vega, J.A. Espinoza Figueroa, A. Cisneros, E. de la Rosa, V.H. Eugenio Lopez, Mendez Garcia, J. Vac Sci. Technol. B 34, 02L110 (2016). https://doi.org/10.1116/1.4942898
44. L.A. Farrow, C.J. Sandroff, M.C. Tamargo, Raman scattering measurements of decreased barrier heights in GaAs following surface chemical passivation. Appl. Phys. Lett. 51, 1931 (1987). https://doi.org/10.1063/1.98304
45. I.E. Cortes Mestizo, E. Briones, C.M. Yee, L. Rendón, L.I. Zamora Peredo, R. Espinosa Vega, V.H. Droopad, Méndez, García, J. Cryst. Growth 477, 59–64 (2017). https://doi.org/10.1016/j.jcrysgro.2017.04.015
46. D. Segev, C.G. Van de Walle, Europhys. Lett. 76(2), 305–311 (2006). https://doi.org/10.1209/epl/i2006-10250-2
47. A. Chtanov, T. Baars, M. Gal, Phys. Rev. B 53(8), 4704 (1996). https://doi.org/10.1103/PhysRevB.53.4704
48. R. Kudrawiec, W. Walukiewicz, J. Appl. Phys. 126, 141102 (2019). https://doi.org/10.1063/1.5111965
49. D.E. Aspnes, Surf. Sci. 37, 418–442 (1973). https://doi.org/10.1016/0039-6028(73)90337-3
50. D.E. Aspens, A.A. Studna, Phys. Rev. B 7(10), 4605–4625 (1973). https://doi.org/10.1103/PhysRevB.7.4605
51. O.S. Komkov, S.A. Khakhulin, D.D. Firsov, P.S. Avdienko, I.V. Sedova, S.V. Sorokin, Semiconductors 54(10), 1198–1204 (2020). https://doi.org/10.1134/S1063782620100176
52. W. Walukiewicz, W. Shan, J.W. Ager III, D.R. Chamberlin, E.E. Haller, J.F. Geisz, D.J. Friedman, J.M. Olson, S.R. Kurtz. (April 1999). Nitrogen-Induced Modification of the Electronic Structure of Group III-N-V Alloys [Conference paper]. Electrochemical Society International Symposium, Seattle, Washington. https://www.nrel.gov/docs/fy99osti/29583.pdf
53. K. Chakir, C. Bilel, A. Rebey, Semiconductors 53, 1740–1744 (2019). https://doi.org/10.1134/S1063782619130037

Publisher's Note Springer Nature remains neutral with regard to jurisdictional claims in published maps and institutional affiliations.

Springer Nature or its licensor (e.g. a society or other partner) holds exclusive rights to this article under a publishing agreement with the author(s) or other rightsholder(s); author self-archiving of the accepted manuscript version of this article is solely governed by the terms of such publishing agreement and applicable law.